Role of grain size in superconducting boron-doped nanocrystalline diamond thin films grown by CVD

Gufei Zhang,[1,*] S. D. Janssens,[2] J. Vanacken,[1] M. Timmermans,[1] J. Vacík,[3] G. W. Ataklti,[1] W. Decelle,[1] W. Gillijns,[1] B. Goderis,[4] K. Haenen,[2,5] P. Wagner,[2,5] and V. V. Moshchalkov[1]

[1]*Insititute for Nanoscale Physics and Chemistry, Katholieke Universiteit Leuven, Celestijnenlaan 200D, B-3001 Leuven, Belgium*
[2]*Institute for Materials Research, Hasselt University, Wetenschapspark 1, B-3590 Diepenbeek, Belgium*
[3]*Nuclear Physics Institute, Academy of Sciences of the Czech Republic, 25068 Husinec-Rez, Czech Republic*
[4]*Molecular and Nanomaterials, Department of Chemistry, Katholieke Universiteit Leuven, Celestijnenlaan 200F, B-3001 Leuven, Belgium*
[5]*Division IMOMEC, IMEC vzw, Wetenschapspark 1, B-3590 Diepenbeek, Belgium*

The grain size dependence of the superconducting transition, the normal state resistivity, and the insulating behavior at high magnetic fields are studied on a series of boron-doped nanocrystalline diamond (B:NCD) thin films with different grain sizes. The systematic change of the grain size is achieved by varying the methane-to-hydrogen ratio (C/H ratio) for the growth of different B:NCD films. Even though a fixed trimethylboron- (TMB) to-methane gas ratio is supposed to induce the identical boron-doping level in all the B:NCD films, the boron concentration and the carrier density are found to be a decreasing function of the grain size. Another consequence of the increase in grain size is the decreasing grain boundary density. These two concurrent consequences of the chemical vapor deposition mode of B:NCD are responsible for the grain size dependence of the critical temperature T_C, the localization radius a_H at the boron site, the normal state resistivity ρ_{norm}, the Hall mobility μ_H, the Ioffe-Regel product $k_F l$, the H_{C2}-T phase boundary, and the coherence length ξ_{GL}.

I. INTRODUCTION

The two main kinds of synthetic diamonds are widely known as HPHT diamond and CVD diamond, denoting the used fabrication method of high-pressure high-temperature (HPHT) synthesis and chemical vapor deposition (CVD), respectively.[1] In comparison with HPHT synthesis, CVD is used to manufacture synthetic diamond in the form of wafers/thin films, offering opportunities to print diamond circuitry and to shape it into other high-tech devices, e.g. CVD diamond microchips. Chemical vapor deposition diamond microchips are feasible since, by introducing certain concentrations of boron, insulating diamond wafers can be transformed into doped semiconductors and/or metal-like conductors (CVD diamond:B).[2,3] Tunable electrical properties, in combination with high hardness and high thermal conductivity, make CVD diamond a candidate for developing new chip materials supporting high-performance computing.[4]

Intrinsic diamond is an insulator. Remarkably, it also shows a high thermal conductivity, which originates from its high phonon frequency. As such, one would seek for phonon-mediated Cooper pairs in diamond through introducing free charge carriers by doping.[5] In 2004, Ekimov *et al.* found type-II superconductivity in boron-doped HPHT diamond.[6] Later on, Takano *et al.* added CVD diamond:B to the list of superconductors as well.[7] From these pioneering works, the community learned that synthetic diamond also provides new opportunities for fundamental research on superconductivity.

As an important subcategory of CVD diamond:B, boron-doped nanocrystalline diamond (B:NCD) thin films have recently attracted a substantial interest. Different from a single crystalline bulk diamond, B:NCD films have a granular morphology, i.e. monocrystalline diamond grains are embedded into a matrix abundant in disordered sp^3 and sp^2 phases.[1,8–12] How can such a system be conducting or even superconducting? How do the grain boundaries influence the

global conductivity or superconductivity? An answer to these questions might shed some light on the understanding of the conduction mechanism in granular and/or strongly disordered conductors and/or superconductors, including granular high T_C superconductors. Although several intense discussions have been already devoted to these issues,[13–19] up to now, a comprehensive study of the influence of the granular morphology on electrical transport has not been so far carried out. In this paper, by presenting our data collected on a set of well-characterized B:NCD thin films with systematic grain size change, we investigate the role of grain size in defining the electrical properties of the superconducting B:NCD films.

II. EXPERIMENT

A. Samples prepared by MPECVD

The B:NCD granular thin films were deposited on isolating fused-silica substrates in an ASTeX 6500 series MPECVD (microwave plasma-enhanced chemical vapor deposition) reactor.[20,21] The silica substrate was firstly seeded with a cap monolayer of detonation diamond powders (Ø $\sim$ 5–10/nm). The seeding-generated nucleation sites have a density of 10^{11} cm^{-2} and are evenly spaced with a relatively narrow inter-grain distance distribution.[20] Afterwards, the seeded substrate was placed into the reactor filled with a conventional CH$_4$/H$_2$ gas mixture. Under irradiation with microwaves, energetic carbon atoms were released from CH$_4$, and diamond islands were growing around the nucleation sites. H$_2$ was employed to etch away sp^2 impurity phases. Boron doping was induced by trimethylboron (TMB) gas injection with a TMB/CH$_4$ ratio of 5000 ppm for all the samples. Through assigning values of 1.5%, 2.0%, 3.0%, 4.0%, and 5.0% to the CH$_4$/H$_2$ ratio (shortened to C/H ratio hereinafter), five different deposition rates were used, producing five samples with systematically changing grain size.[21,22] The B:NCD films with approximately

the same thickness of 150 ± 10 nm are labeled according to their C/H ratios, respectively.

B. Grain size determined by SEM and XRD

The granular morphology of the B:NCD films was characterized by scanning electron microscopy (SEM). Digital processing of the SEM images was performed by Matlab to obtain the grain size statistics over the sample surfaces.

X-ray diffraction (XRD) was used to determine the mean size of the columnar diamond grains. The XRD spectra were collected with a horizontal Geigerflex diffractometer in the reflection mode (Bragg–Brentano geometry) mounted on a Rigaku RU-200B rotating Cu-anode ($\lambda = 1.542$ Å) at a power of 4 kW. The widths of the divergence, receiving, and scattering slits were $2°$, 0.15 mm, and $0.5°$, respectively. The diffracted Cu Kα x-ray photons were collected after Ni filtering on a scintillation counter.

C. Electrical transport properties measured in Heliox and PPMS

The B:NCD films were patterned into six-arm Hall bars for transport measurements. Longitudinal thermoresistivity $\rho_{xx}(T)$ and magnetoresistivity $\rho_{xx}(B)$ in the temperature range from 0.4 to 7 K were measured in a Heliox ^{3}He cryostat from Oxford Instruments, equipped with a 5-Tesla dc magnet. The $\rho_{xx}(T)$ curves in the temperature range of 2–270 K were measured in a Quantum Design physical property measurement system (PPMS). Between 2 and 7 K, the $\rho_{xx}(T)$ curves, taken in these two different cryostats, perfectly overlap with each other. Hall-effect measurements (HEM) at 2 and 270 K were performed by using the PPMS. The magnetic fields, used for the measurements of thermoresistivity, were applied perpendicular to the film surface.

D. Boron concentration n_{Boron} (carrier density n_{QP}) determined by NDP (HEM)

The nondestructive nuclear analytical method, neutron depth profiling (NDP), was employed to measure the depth dependence of the boron concentration n_{Boron}. The profiling is based on the thermal neutron-induced ^{10}B$(n,\alpha)^7$Li reaction occurring on the ^{10}B isotope. With the help of the aforementioned six-arm Hall bars, the quasiparticle (QP) density n_{QP} was determined by HEMs.

III. RESULTS AND DISCUSSION

A. Grain size tuned by the C/H ratio

Figure 1 shows the systematic change in grain size of the samples, revealing the influence of the C/H ratio on the B:NCD growth rate. Scanning electron microscopy images, taken on Sample 1.5%–Sample 5.0%, are presented in Fig. 1(a) to give an overview of the granular morphology and the grain size difference between the samples. As shown in Fig. 1(b), digital processing of these SEM images yields statistics of the grain sizes for each sample, and the grain size distributions are found to be lognormal [see the fitting curves in red/dark gray in Fig. 1(b)]. The inverse of the mean grain sizes deduced from the lognormal fittings, $1/D$, is found to be a linearly increasing
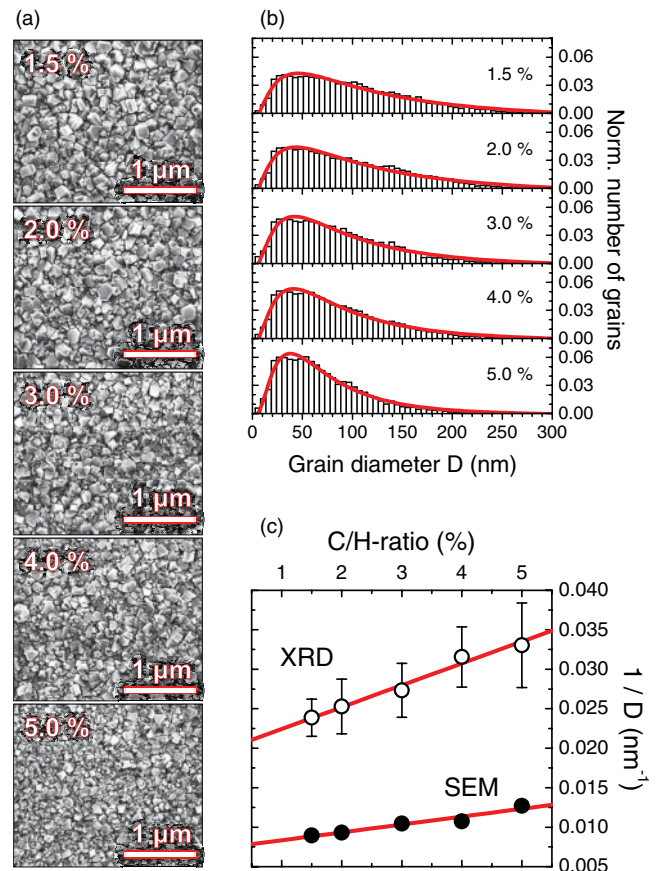
FIG. 1. (Color online) Mean grain sizes of the B:NCD thin films derived from scanning electron microscopy (SEM) and x-ray diffraction (XRD) measurements. (a) Granular morphologies of Sample 1.5%–5.0% characterized by SEM. (b) Grain size statistics obtained from the SEM images (hollow bars in black) are fitted to lognormal distributions (solid curves in red/dark gray). (c) The reverse mean grain size $1/D$ as derived from the SEM (filled circles) and XRD (hollow circles) data are found to be a linear function of the C/H ratio.

function of the C/H ratio [see the filled circles in Fig. 1(c)], indicating that a higher C/H ratio leads to a higher deposition rate and to a smaller mean grain size.[21,23]

Since SEM solely provided us the grain size statistics over the film surface, XRD was utilized to determine the mean size of the columnar diamond grains. The most intense (111) peak profiles were adopted to deduce the mean grain sizes, according to the Scherrer formula. As shown in Fig. 1(c), although the so-calculated $1/D$ is also a linearly increasing function of the C/H ratio (see the open circles), the numerical values are about 2.7 times larger than the data extracted from SEM. This difference seems to originate from the inverted pyramid-like growth mode of the columnar diamond grains.[11,12,21,24,25] The SEM images were taken on the film surface which is assembled by the top bases of the inverted pyramids. X rays, penetrating through the film, were diffracted from the whole pyramids. In this sense, our SEM and XRD data, complementary to each other, give the information about the growth mode of B:NCD.
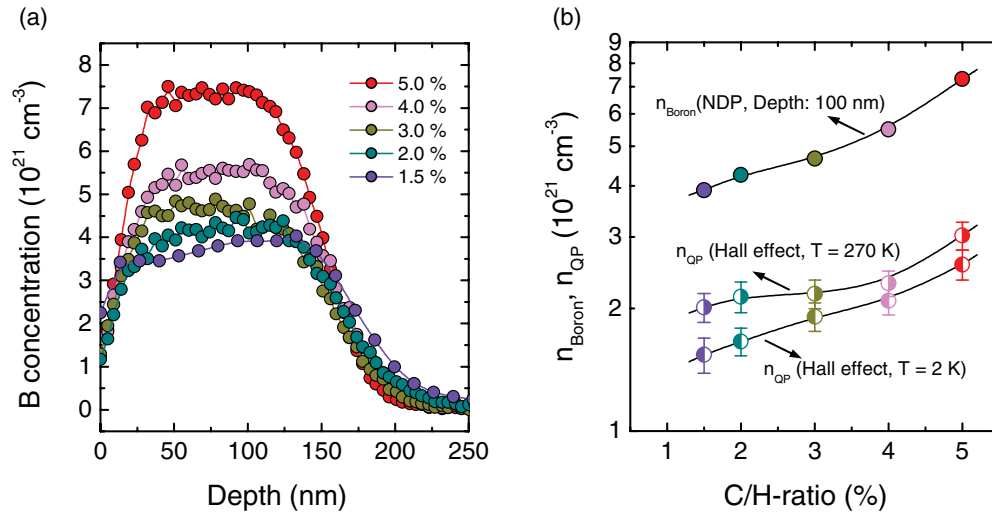
FIG. 2. (Color online) Boron concentration (n_{Boron}) and charge carrier density (n_{QP}) derived from neutron depth profiling (NDP) and Hall-effect measurements (HEM), respectively. (a) Here, n_{Boron} determined by NDP (after Ref. 21). (b) The C/H ratio dependence of n_{Boron} and n_{QP}. Here, n_{QP} determined by HEM is plotted together with the 100-nm-deep NDP data to interpret the boron doping efficiency.

B. Grain size dependent n_{Boron} and n_{QP}

As mentioned above, the TMB gas injection into the reactor was with a TMB/CH$_4$ ratio of 5000 ppm, the same for all five samples. Accordingly, the same n_{Boron} value was expected for all samples (Sample 1.5%–Sample 5.0%). However, this expectation was not supported by NDP measurements. Figure 2 presents the grain size dependence of n_{Boron} and n_{QP}, derived from NDP and HEM, respectively. The depth profiles of n_{Boron} are plotted in Fig. 2(a). Despite the fixed TMB/CH$_4$ ratio, n_{Boron} in the films is found to increase with the C/H ratio. Neutron depth profiling data also confirms the same film thickness (150 ± 10 nm) of the samples.

In order to determine the doping efficiency of boron, we also performed the HEM studies. The HEM-determined n_{QP} is plotted as a function of the C/H ratio in Fig. 2(b), together with the 100-nm-deep n_{Boron} (after Ref. 21). The grain size dependence of n_{QP} is with the same tendency as that of n_{Boron}. It is quite evident that there is a substantial difference between the total boron concentration and the charge carrier (quasiparticle) density. The n_{QP} value taken at 2 K is about 2.7 times smaller than n_{Boron}, meaning that merely 37% of the boron dopants contribute to the electrical transport at 2 K by generating mobile charge carriers. As temperature increases, the poor ionization efficiency of the deep-level boron dopants gets improved, and the difference between n_{Boron} and n_{QP} becomes less pronounced, e.g. at 270 K, approximately 50% of the boron dopants create mobile carriers.

The increasing C/H ratio leads to decreasing D and increasing n_{Boron} and n_{QP}. Within a fixed area, a decrease in the mean grain size D results in the growth of the grain boundary density. An increase in the amount of methane triggers an increase in the deposition rate and a decrease in the hydrogen ration. As a consequence, samples with smaller grain size are richer in grain boundaries containing disordered sp^3 and sp^2 phases.[1,8–12] Consequently, incorporation of defects, including boron dopants, is better in these samples.[21]

C. Grain size dependence of the superconducting transition

The B:NCD films with n_{Boron} ranging from 4.2×10^{21} cm^{-3} to 7.3×10^{21} cm^{-3}, on the metallic side of the metal-to-insulator transition (MIT, $n_{\mathrm{Boron}} \sim 2 \times 10^{20}$ cm^{-3}), show superconductivity at low temperatures. Figure 3 presents their superconducting transitions (SCTs) found in resistivity measurements. The $\rho_{xx}(T)$ curves, taken at zero field and at 5 T, are plotted together in Fig. 3(a) to indicate the onset and offset of the transitions. As shown in Figs. 3(b) and 3(c), three characteristic temperatures, i.e. the onset temperature T_C^{onset} above which $\rho_{xx}(T)|_{B=0\mathrm{T}}$ and $\rho_{xx}(T)|_{B=5\mathrm{T}}$ merge into one curve, the critical temperature T_C^{mid} at the midpoint of the transition, and the offset temperature T_C^{offset} below which $\rho_{xx} = 0$, are derived from Fig. 3(a) to describe the SCTs.

It is clearly seen from Fig. 3(b) that the larger the C/H ratio (the smaller the grain size), the higher the characteristic temperatures T_C. Taking into account the grain size dependence of n_{QP} [see Fig. 2(b)], this phenomenon is easily understood from the data shown in Fig. 3(c) as T_C is enhanced by increasing n_{QP}.[26] Another interesting feature of the T_C vs C/H ratio dependence is the broadness $\Delta T_C = T_C^{\mathrm{onset}} - T_C^{\mathrm{offset}}$ of the SCTs, which is clearly increasing with the C/H ratio. This phenomenon is related to the superconducting condensation mode of B:NCD. Recently, Willems *et al.*[25] and Dahlem *et al.*[27] found strong spatial modulation of the superconducting order parameter 2Δ in B:NCD films. These local studies confirm that the global superconductivity in B:NCD films exists due to the phase locking between different superconducting droplets. Moreover, the insulating state of the parent substance (NCD) and the fact that doping with boron results in a superconducting state also supports the idea of this superconducting droplet formation.[28] In our samples, as the grain size D decreases, the increasing grain boundary density will complicate the phase locking between superconducting droplets, and this could hinder the formation of the superconducting path $\rho_{xx} = 0$ throughout the whole sample.
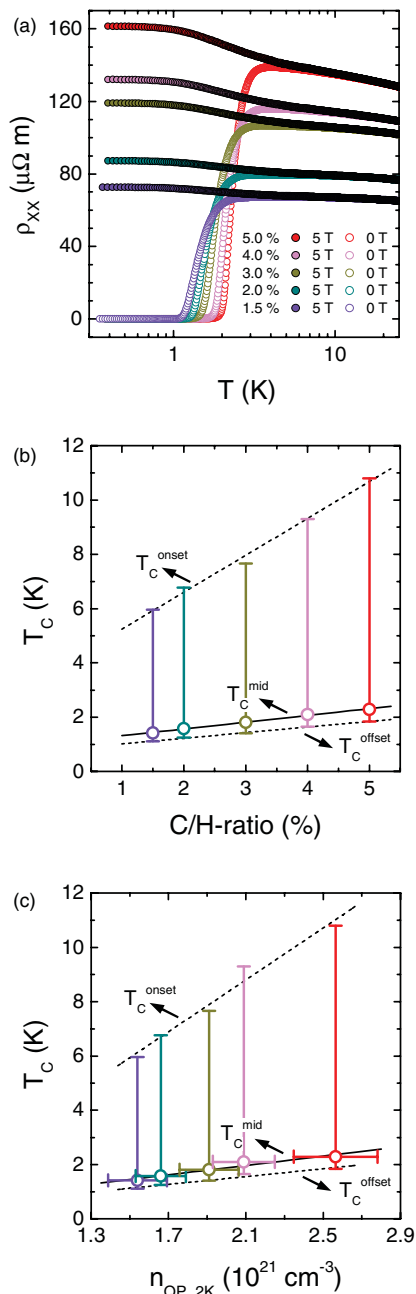
FIG. 3. (Color online) The C/H ratio (grain size) dependence of the superconducting transition in the B:NCD films. (a) The temperature dependence of the longitudinal resistivity at zero field and at 5 T. (b) The C/H ratio dependent superconducting transitions characterized by the critical temperature T_C^{mid} (hollow circles), the onset temperature T_C^{onset} (upper limits of the error bars), and the offset temperature T_C^{offset} (lower limits of the error bars). The solid and dashed lines are guides to the eye, denoting the C/H ratio dependence of T_C^{mid}, T_C^{onset}, and T_C^{offset}, respectively. (c) The carrier density (n_{QP}) dependence of the characteristic temperatures [data plotted in the same way as in Fig. 3(b)].

D. Influence of the grain size on the insulating and dirty metallic normal states

The B:NCD films undergo a superconductor-dirty metal transition when heated through T_C^{onset}. The normal state

of superconducting B:NCD is generally considered as dirty metallic,[3,13,15,16,18,19,24] since the free motion of charge carriers is strongly perturbed by various intragrain defects and grain boundaries, and the delocalization of these intragrain charge carriers by thermal activation will lead to a negative $d\rho_{xx}/dT$ and a resistivity change $\Delta\rho_{xx}|_{per10K} < 10\%$.[29–32] Figure 4(a) shows the dirty metallic (or weakly insulating) behavior observed in our B:NCD films. The $\rho_{xx}(T)|_{B=5T}$ curves, following exponential decay above T_C^{onset}, all have different $d\rho_{xx}/dT$ values. The smaller the grain size, the larger the absolute value of $d\rho_{xx}/dT$, e.g. we observe the largest $|d\rho_{xx}/dT|$ for Sample 5.0% and the smallest $|d\rho_{xx}/dT|$ for Sample 1.5%. Assuming that all intergrain potential walls are with the same height and that the attempt frequency of a quasiparticle hopping over the walls stays constant, the $|d\rho_{xx}/dT|$ value will be then controlled by the number of the intergrain barriers. One might argue that despite the highest grain boundary density, Sample 5.0% also has the largest n_{QP}, which may compensate the negative influence of the grain boundaries on the conductivity. However, in our B:NCD thin films, this compensation is obviously insufficient. The dominant influence of the grain boundaries also results in the increasing normal state resistivity ρ_{norm} vs the decreasing grain size.

In the presence of a high magnetic field $B = 5$ T, the B:NCD films undergo a metal-insulator transition when cooled through T_C^{onset}. The insulating states with $\Delta\rho_{xx}|_{per10K} \gg 10\%$ are indicated in Fig. 4(a) by a dash-dotted box, within which the fermion hopping mechanism (FHM) should be taken into account to analyze the hopping conductivity.[18,33] As shown in Fig. 4(b), plotting the $\rho_{xx}(T)|_{B=5T}$ curves as a function of $1/T^{0.25}$ on a semilogarithmic scale, the low temperature segments (1–8 K) of the curves are found to be in a good agreement with the variable range hopping model (VRH, Mott's law in three dimensions)

$$\rho = \rho_0 \exp\left\{\left(\frac{T_0}{T}\right)^{\frac{1}{4}}\right\} \qquad (1)$$

where T_0 characterizes the strength of the quasiparticle correlation.[34,35] It is also noted that, on the semilogarithmic scale, the slope S of the linear VRH fittings, given by

$$S = T_0^{1/4}\log_{10}e, \qquad (2)$$

slightly but systematically increases when decreasing the grain size. This observation enables us to explore the grain size dependence of the S-related localization radius $a_H \sim T_0^{-1/3}$ of boron dopants.

For doped semiconductors, e.g. diamond:B, thermal activation dominates the hopping conductivity at high temperatures, and in principle, the hopping scenario should be the so-called next neighbor hopping (NNH) (practically, for B:NCD, this law only holds within a relatively narrow temperature range, namely at very high temperatures, where the potential barriers of the grain boundaries are negligible[11,12,24]). However, as the temperature decreases, this NNH dominance will be shared with another important mechanism, i.e. the overlapping of the localized carrier wave functions.[35] The a_H, denoting the decay length of the localized carrier wave function and deduced via the above-mentioned VRH fittings, is plotted in Fig. 4(c) as a function of the C/H ratio. It is found that a B:NCD film with
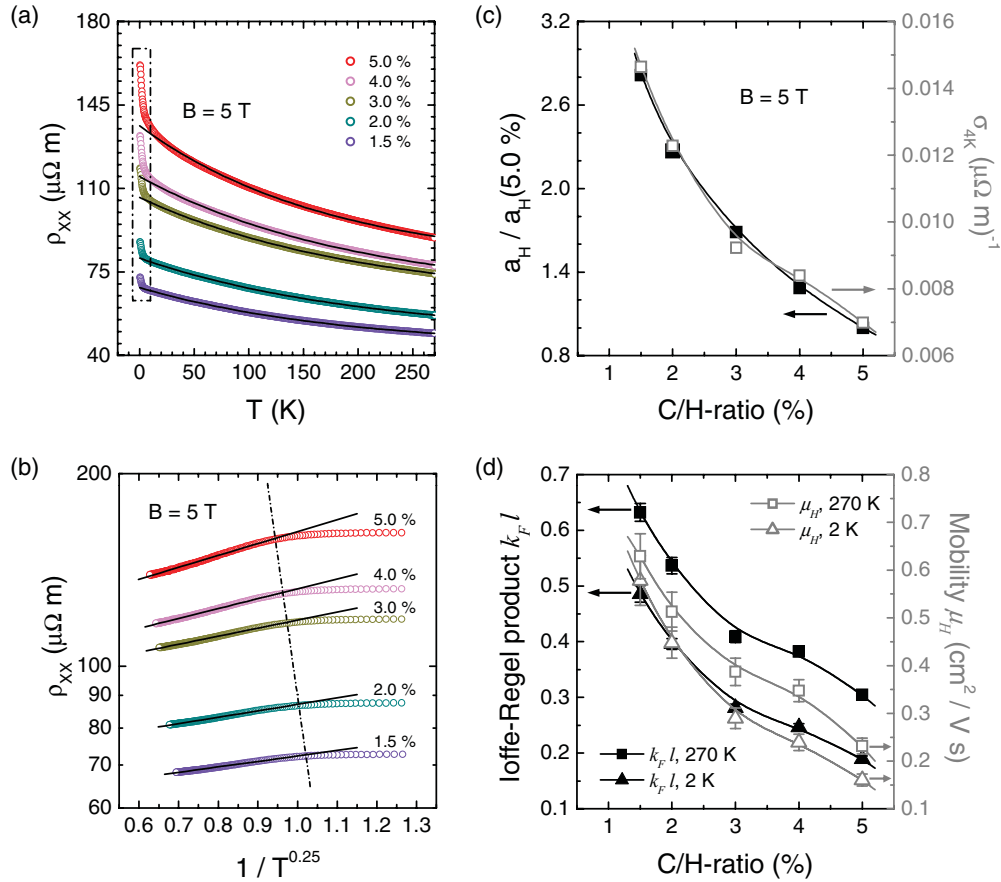
FIG. 4. (Color online) The insulating and dirty metallic normal states of the B:NCD films with systematic change in grain size. (a) The temperature dependence of the longitudinal resistivity at 5 T. Here, $\rho_{xx}(T)|_{B=5T}$ curves taken from 270 K down to 0.4 K are plotted to illustrate the dirty metal-insulator transition. In the dirty metallic state from 270 K to T_C^{onset}, the thermoresistivity follows an exponential decay as fitted by the solid curves in black. When cooled through T_C^{onset}, the $\rho_{xx}(T)|_{B=5T}$ curves deviate from the exponential decay, and the B:NCD films enter the insulating state as indicated by a dashed box. (b) The insulating states [see the dashed box in Fig. 4(a)] characterized by the fermion hopping mechanism (FHM). The low-temperature segments ($<T_C^{\text{onset}}$) of the $\rho_{xx}(T)|_{B=5T}$ curves are plotted vs $1/T^{0.25}$ on a semilogarithmic scale. On the left side of the dashed line, the $\rho_{xx}(T)|_{B=5T}$ curves are in a good agreement with the variable range hopping law (VRH). (c) The C/H ratio dependence of the localization radii deduced from the VRH fittings follows the same tendency as that of σ_{4K} vs C/H ratio. (d) The C/H ratio dependence of the Ioffe–Regel product $k_F l$.

a smaller grain size also has a smaller a_H, although its n_{Boron} and n_{QP} are higher. The hopping conductivity in the insulating state, e.g. σ_{4K} as plotted in Fig. 4(c), shows the same grain size dependence as a_H does. The grain-size-dependent localization of the charge carriers is hereby evidenced.

Our arguments based on the longitudinal resistivity measurements $\rho(T)$ are then confirmed by Hall-effect studies. Figure 4(d) presents the grain size dependence of the Ioffe–Regel product

$$k_F l = \frac{\hbar(3\pi^2)^{2/3}}{e^{5/3}}\frac{R_H^{1/3}}{\rho} \qquad (3)$$

where k_F denotes the Fermi wavenumber, l represents the elastic mean free path of the carriers, R_H is the Hall coefficient, and ρ stands for the resistivity.[36] The values $k_F l < 1$ indicate the localization of the charge carriers since, for a carrier wave with mean free path l shorter than wavelength λ_F, wave propagation becomes impossible. The smaller the grain size is, the more distinct the localization becomes. We can also see

that at high temperature $T = 270$ K, the value of $k_F l$ is higher and it approaches 1, thus suggesting an effective annihilation of the intergrain potential barriers. This effective annihilation is caused by the enhanced thermal activation energy and/or the increased n_{QP} [see Fig. 2(b)]. The Hall mobility μ_H is also plotted in Fig. 4(d) as an additional parameter characterizing the grain size dependent localization.

E. An overview of the conduction mechanisms in B:NCD films

In the preceding sections, we presented the grain size dependence of various characteristic parameters extracted from the electrical transport measurements and gave an interpretation of the transport properties based on the competition between n_{QP} and the grain boundary density. Nevertheless, there are still a few questions to be answered. (1) As shown in Figs. 3 and 4, below T_C^{offset}, the superconducting condensation (the steep decrease in $\rho_{xx}(T)|_{B=0T}$) and the insulating transition (the sudden increase in $\rho_{xx}(T)|_{B=5T}$) take place nearly at the same position. What is the origin of this phenomenon?
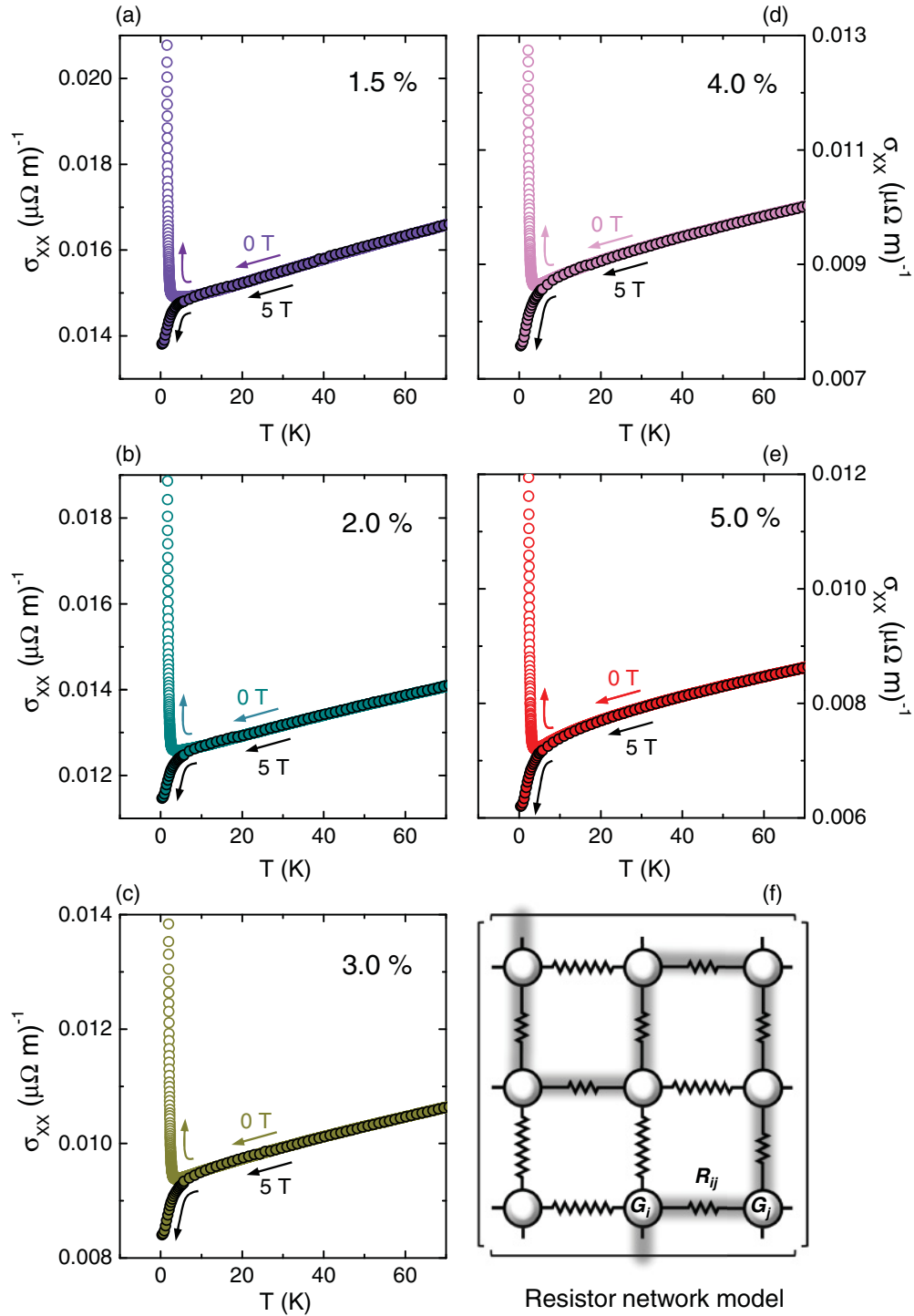
FIG. 5. (Color online) The conduction mechanisms in B:NCD and the resistor network model. (a)–(e) The temperature dependence of the inverse resistivity measured at zero field and at 5 T on Sample 1.5%–Sample 5.0%. (b) Based on Figs. 5(a)–5(e), the B:NCD films are schematically transformed into a resistor network in which a percolation/condensation path is highlighted by a glowing polyline in gray. A unit of the network, composed of Grain G_i, Grain G_j, and their intergrain resistor R_{ij}, is denoted for the conduction mechanism analysis.

(2) In the temperature range of 1–8 K, the global insulating state is achieved by applying a 5-T magnetic field, and the hopping conduction corresponds to VRH. However, this global insulating state of B:NCD in 5 T assumes the breakdown of the $\rho_{xx} = 0$ condensation path rather than the complete breakdown of all the Cooper pairs. In other words, owing to the granular morphology of B:NCD, superconducting droplets most probably may survive in the insulating matrix.[37] In this sense, how will the local superconducting band gaps influence the fermion hopping conduction? (3) Below 1 K, the $\rho_{xx}(T)|_{B=5T}$ curves deviate from the VRH fittings and flatten out. What could be the cause of this interesting feature? Are there contributions

from the preserved superconducting droplets? An overview of the conduction mechanisms involved in B:NCD transport properties can assist us in answering these questions.

To have an insight into the conduction mechanisms involved in the superconducting states, the insulating states, and the dirty metallic states, the reverse resistivities of the samples taken at 0 and 5 T are plotted as a function of temperature in Figs. 5(a)–5(e). As shown in Figs. 5(a)–5(e), when decreasing the temperature down to the onset temperature of $T_C{}^\text{onset}$, the $\sigma_{xx}(T)|_{B=0\text{T}}$ and $\sigma_{xx}(T)|_{B=5\text{T}}$ curves follow the same decreasing dependence. Below $T_C{}^\text{onset}$, a steep increase in $\sigma_{xx}(T)|_{B=0\text{T}}$ and simultaneously, a sudden decrease in $\sigma_{xx}(T)|_{B=5\text{T}}$ appear. When $T < T_C{}^\text{onset}$ and $B = 0$ T, the formation of intragrain Cooper pairs and the onset of intergrain phase locking of the superconducting order parameters provide the superconducting channel for transport.[38,39] When $T < T_C{}^\text{onset}$ and $B = 5$ T, the majority of the intragrain Cooper pairs are suppressed, and the intergrain phase locking is broken. Consequently, the conductivity channel is dominated by the large intergrain resistance (the grain boundaries), which explains the sudden drop in $\sigma_{xx}(T)|_{B=5\text{T}}$.

Based on these observations, we can conclude that in B:NCD, the intergrain resistance is much higher than the intragrain resistance. This conclusion enables us to come up with the resistor network model, as shown in Fig. 5(f),[40,41] which is in a qualitative agreement with the growth mode of nanocrystalline CVD diamonds. During the growth of an individual grain, energetic carbon atoms epitaxially settle down on the facets of a diamond nucleation seed, and hence perfect sp^3 lattice can be built up with substitutional boron dopants insides. However, owing to the inevitable randomness of the positions and orientations of the diamond nucleation seeds, lattice mismatch always exists between neighboring grains. The grain boundaries are, therefore, abundant in disordered sp^3 and sp^2 phases, in which boron atoms act as deep-level impurities without contributing mobile charge carriers to electrical transport.[1,8–12]

The superconducting state at $T < T_C{}^\text{onset}$ and $B = 0$ T can be represented by taking a unit cell of the resistor network, i.e. the grains of G_i and G_j together with their intergrain resistor R_{ij} [see Fig. 5(f)], as an example. When decreasing the temperature below $T_C{}^\text{onset}$, superconducting gaps $2\Delta_i$ and $2\Delta_j$ open up in G_i and G_j, respectively. Restricted by R_{ij} in between, phase locking between the superconducting order parameters of $2\Delta_i$ and $2\Delta_j$ generates a weak junction with current tunneling through R_{ij}, which is known as Josephson junction. As a complex of abundance of Josephson junctions,[38,39] the nanocrystalline diamond film does not undergo the superconducting transition abruptly. Its resistivity does not drop to zero until the complete onset of a superconducting path in which intragrain superconducting order parameters are phased-locked together.[38,39] This process results in the relatively broad superconducting transitions in B:NCD films, i.e. $T_C{}^\text{onset}$ lies far above $T_C{}^\text{offset}$, and a strong magnetic field dependence of the transitions.[18] The decreasing B:NCD grain size will lead to the appearance of additional connections in the Josephson junction arrays, and hence this may result in broader superconducting transitions (see Fig. 3).

Below $T_C{}^\text{onset}$, the superconductor-insulator transition from $\sigma_{xx}(T)|_{B=0\text{T}}$ to $\sigma_{xx}(T)|_{B=5\text{T}}$ is driven by magnetic field. More

than breaking the phase locking between $2\Delta_i$ and $2\Delta_j$, depending on its magnitude, the applied magnetic field also reduces and/or closes the superconducting gaps of $2\Delta_i$ and $2\Delta_j$ in G_i and G_j, respectively. Upon shrinking $2\Delta_i$ and $2\Delta_j$, the quasiparticles are released. Localized by the adjacent intergrain resistors, these quasiparticles released from the intragrain superconducting droplets are still not fully free. In this sense, B:NCD grains with such quasiparticles confined inside can be considered as sort of very big impurity atoms incorporated into the resistor network, as shown in Fig. 5(f), e.g. G_i and G_j.

Based on this type of resistor network model, with the so-called dimensionless percolation method,[40] a phenomenological analysis of the hopping conduction in B:NCD films is straightforward, which justifies our use of the VRH law in fitting of the $\rho_{xx}(T)|_{B=5\text{T}}$ curves [see Fig. 4(b)]. For a resistor network, as shown in Fig. 5(f), its characteristic resistivity is determined by the resistivity of the critical percolating path (see the line in gray glow):

$$\rho \sim \exp\{\xi_C\}. \tag{4}$$

The dimensionless variable ξ takes into account the presence of possible conductivity channels enabling the percolation, e.g. conductivity channels arising from wave function overlapping and from thermal activation, etc. When the critical percolating path is established, $\xi = \xi_C$. The exponentially wide range of the resistors of the network formulated in Eq. (4) works well in all cases of strongly inhomogeneous media.[40] Referring to Fig. 5(f), for instance, there are two impurity atoms G_i and G_j participating in the hopping process. The distance and energy difference between G_i and G_j are r_{ij} and E_{ij}, respectively. At low temperatures ($T < T_C{}^\text{onset}$), where both wave function overlapping and thermal activation are important, the dimensionless variable ξ can be written as

$$\xi \equiv \frac{r_{ij}}{a_H} + \frac{E_{ij}}{k_B T}. \tag{5}$$

The first term in the right of Eq. (5) brings r_{ij} into comparison with the localization radius of a_H, while the second item gives us a contribution corresponding to how much energy the system gains by increasing the temperature to overcome the difference E_{ij}.[35,40,42,43] Through the combination of the resistor network model Eq. (4) and the percolation theory Eq. (5), we obtain

$$\rho \sim \exp\left\{\frac{(r_{ij})_C}{a_H}\right\} \exp\left\{\frac{(E_{ij})_C}{k_B T}\right\}, \tag{6}$$

The first exponential factor in Eq. (6) arises from the overlap of two hydrogen-like wave functions centered at G_i and G_j, respectively. The second exponential factor, taking into account both the equilibrium Planck distribution function around the Fermi level and the energy level occupancy of G_i and G_j, provides the number of states whose energies are concentrated in a narrow band near the Fermi level.[40]

To deduce the characteristic resistivity ρ of the network, as expressed in Eq. (4), the critical percolating path ξ_C needs to be found first from the general percolation condition of

$$VN = B_C^{(3D)} \tag{7}$$

with $B_C^{(3D)}$ being a constant depending only on dimensionality (3D in the case of our B:NCD films), V being the characteristic volume $V = 4\pi r_{ij}^3/3$, and N being the number of giant impurity atoms taking part in the conduction process,

$$N = \int g(E) dE \sim \int |E - E_F|^n \, dE \sim (E_{ij})^{n+1} \qquad (8)$$

where $g(E)$ is the density of states in the vicinity of the Fermi energy E_F, and n describes the shape of $g(E)$ around E_F ($n = 0$ for Mott's law in 3D).[35,43] When increasing the temperature, closure of the superconducting gaps of $2\Delta_i$ and $2\Delta_j$ ensures a nonzero $g(E)$ for the integral in Eq. (8). At $\xi = \xi_C$,

$$\frac{4\pi (r_{ij})_C^3}{3} (E_{ij})_C^{n+1} \sim B_C^{(3D)}. \qquad (9)$$

According to Eq. (5), we have

$$(r_{ij})_C \sim \xi_C a_H \qquad (10)$$

and

$$(E_{ij})_C \sim \xi_C k_B T. \qquad (11)$$

Inserting Eqs. (10) and (11) and $n = 0$ into Eq. (9), the critical percolating path ξ_C can be found,

$$\xi_C \sim \left(\frac{\text{const.}}{a_H^3 T} \right)^{1/4}. \qquad (12)$$

By now, coming back to Eq. (9), the temperature dependence of the characteristic resistivity in Eq. (4) can be deduced as

$$\rho \sim \exp\{\xi_C\} \sim \exp\left\{ \left(\frac{T_0}{T} \right)^{1/4} \right\} \qquad (13)$$

with

$$T_0 = \frac{\text{const.}}{a_H^3}. \qquad (14)$$

The good agreement between the experimental data and Eq. (13) or Eq. (1) in Fig. 4(b) and the so-deduced a_H values decreasing as the grain size decreases [see Fig. 4(c)] suggests that the above-mentioned giant impurity-doped resistor network model seems to be reasonable.

The aforementioned case is for increasing the temperature towards T_C^{onset} ($B = 5$ T). On the other hand, when decreasing the temperature below T_C^{onset} ($B = 5$ T), the superconducting gaps $2\Delta_i$ and $2\Delta_j$ will open up,[25,27] and finally, at lower temperatures, generate a zero $g(E)$ for the integral of Eq. (8), meaning that the quasiparticles taking part in the conduction process are absorbed as Cooper pairs into the superconducting droplets.

The fermion hopping mechanism analyzed above, gives us a general understanding of the hopping conductivity which dominates $\sigma_{xx}(T)|_{B=5T}$ when $T < T_C^{\text{onset}}$. However, this dominance fades away at even lower temperatures around 1 K [see Fig. 4(b)]. As shown in Fig. 4(b), below 1 K, the $\rho_{xx}(T)|_{B=5T}$ curves bend over and flatten out. A rational and possible explanation for this observation is that, within the temperature range of 0.3–1 K, several sorts of mechanisms balance out. Besides VRH, another mechanism, which may increase $\rho_{xx}(T)|_{B=5T}$ when decreasing the temperature, is

orbital shrinking of impurity states in boron atoms in high magnetic field.[26] In our case, technically $B = 5$ T might not be considered as a sufficiently high field for that. Nevertheless, if taking into account the ratio of $B/T = 5$ T/0.3 K $\approx$ 17 T/K and the relatively low T_C of the samples, the magnetic field could be still effectively high. On the other hand, there are also a few mechanisms which may decrease $\rho_{xx}(T)|_{B=5T}$, e.g. Andreev reflection at the interfaces between the preserved intragrain superconducting droplets and the intragrain metallic regions[43,44] and interference effects in field.[43,45–47]

Nearly half a century ago, Anderson pointed out that interference between scattered charge waves in a disordered medium cannot be neglected. For a charge carrier traveling along a self-crossing path, the wave propagations going clockwise and counterclockwise will constructively interfere with each other, and hence this interference effect is with a higher probability.[43,48,49] Having a closer look at Fig. 5(f), one can imagine for the metallic grains surrounded by adjacent intergrain resistors how significant this interference effect could be. The interference will reduce the mean free path of the quasiparticles and lower the conductivity. However, when a strong magnetic field is applied perpendicular to the plane of the self-crossing path, a phase difference will be generated between the clockwise propagating path and the counterclockwise propagating one. Consequently, the phase coherence will be broken, and quasiparticles will be delocalized.[43,45–47] Our used fields $B = 5$ T below 1 K may be capable of accomplishing this delocalization.

The flattening-out/saturation of the $\rho_{xx}(T)|_{B=5T}$ curves at low temperatures could also be explained according to the Josephson junction network (JJN) model in the insulating regime.[38,39] Kalok *et al.*[50] recently observed a similar saturation of the sheet resistance in disordered TiN thin films, which was attributed to a low-temperature phase of the charge Berezinskii–Kosterlitz–Thouless (BKT) transition.[38,39,50,51]

The dirty metallic behavior of the B:NCD films can be found in Figs. 5(a)–5(e) when $T > T_C^{\text{onset}}$. High temperature suppresses the remanent superconductivity (closes the phase fluctuation zone) completely by decoupling the precursor Cooper pairs, and all the released intragrain quasiparticles participate in the intragrain conduction.[18] Referring to Fig. 5(f), the network will look like a resistor matrix with metallic grains embedded inside. By then, intergain fermion hopping is not the only contribution to the global conductivity. As aforementioned, an abundance of boron atoms settle at the grain boundaries as deep-level impurities without contributing mobile charge carriers to the electrical transport, on which our resistor network model is based. However, when increasing the temperature above T_C^{onset}, thermally excited deep-level boron impurities could create mobile charges. The doping efficiency can be, therefore, enhanced even by 13% [see Fig. 2(b)]. Accordingly, at high temperatures, our resistor network will transform into a semiconductor network. Naturally, at the semiconducting grain boundaries which separate the metallic grains from each other, Schottky barriers may form. Both thermally assisted fermion hopping over the potential barriers and tunneling through the barriers are possible. These conductivity channels result in the negative thermoresistivity
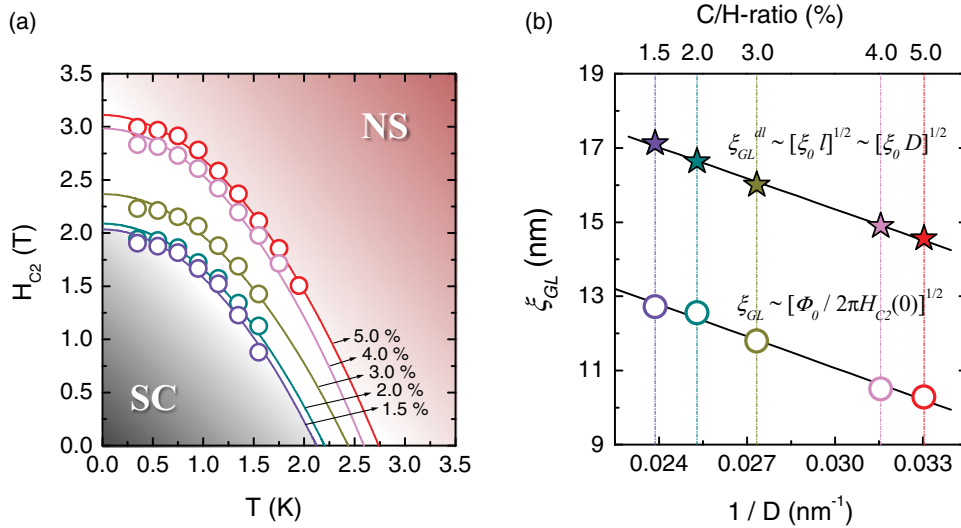
FIG. 6. (Color online) (a) The H_{C2}-T phase boundaries of Sample 1.5%–5.0%, extracted from magnetoresistivity measurements (not shown). (b) The reverse grain size dependence of the Ginzburg–Landau coherence length.

of the dirty metallic diamonds at high temperatures [see Fig. 4(a)].

F. Grain size dependence of the upper critical field H_{C2}

The H_{C2}-T phase boundaries of the B:NCD films are derived from the longitudinal magnetoresistivity $\rho_{xx}(B)$ measurements below T_C. Figure 6(a) presents the grain size dependence of the H_{C2}-T phase boundary. The smaller the grain size, the higher the carrier density n_{QP}, and the higher the critical temperature T_C, with higher upper critical field H_{C2}. It is well known that, for B:NCD, its superconducting transition in the ρ_{xx}-B plane is pretty broad, meaning that it is relatively easy to break down the $\rho_{xx} = 0$ path while difficult to fully suppress the superconducting fluctuations.[5,7,12,15–19] This is the reason why high-valued $H_{C2}(0\,\mathrm{K})$ is always found as in our set of B:NCD films. Sharp edges of multiple facets preserve the remanent superconductivity until a high enough magnetic field is applied to close the superconducting fluctuation region. In the H_{C2}-T plane [see Fig. 6(a)], one can say that the increasing grain size of B:NCD is shrinking the superconducting volume.

As shown in Fig. 6(a), by extrapolating the quadratic fits of the H_{C2}-T phase boundaries down to $T = 0\,\mathrm{K}$, $H_{C2}(0\,\mathrm{K})$ of the samples is found to range from 2 to 3.1 T. According to the relation $\xi_{GL} = [\Phi_0 / 2\pi\,H_{C2}(0\,\mathrm{K})]^{1/2}$ with $\Phi_0 = h/2e$ being the flux quantum, the Ginzburg–Landau coherence length ξ_{GL} is derived and plotted in Fig. 6(b) as a function of the inverse mean grain size $1/D$.[52] As a reference in Fig. 6(b), we also plot the Ginzburg–Landau coherence length in the dirty limit $\xi_{GL}^{dl} \sim (\xi_0 l)^{1/2}$ with ξ_0 being the coherence length of a clean monocrystalline diamond and l being the mean free path.[53] Since, to our knowledge, no data of the coherence length of clean monocrystalline superconducting diamond has so far been collected, a $\xi_0 \sim 7$ nm, which we just obtained on a

polycrystalline bulk diamond, is used here for a rough estimate. Besides, $l \sim D$ is used for an upper limit estimation of the mean free path. As shown in Fig. 6(b), the linear relationship between ξ_{GL} and $1/D$ is parallel to the ξ_{GL}^{dl} vs $1/D$ plot, which suggests the restricting effect of the grain size on the coherence length.

IV. CONCLUSION

By studying the structural and transport properties of a set of B:NCD films with a systematic change of the mean grain size, we have observed the grain size dependence of the critical temperature T_C, the boron localization radius a_H, the normal state resistivity ρ_{norm}, the Hall mobility μ_H, the Ioffe–Regel product $k_F l$, the upper critical field H_{C2}, and the coherence length ξ_{GL}. These consistent observations have been interpreted according to the competition between two concurrent events, i.e. the increasing carrier density n_{QP} and the increasing grain boundary density, when decreasing the mean grain size. The growing carrier density n_{QP} leads to the increasing T_C. The increasing grain boundary density results in lowering a_H, increasing ρ_{norm}, decreasing μ_H and $k_F l$. The increasing H_{C2} can be caused by the growth of n_{QP} and T_C and/or stronger remanent superconductivity in samples with smaller mean grain size. Based on these findings, a general overview of the conduction mechanisms in B:NCD is given on the basis of the resistor network model.

*gufei.zhang@fys.kuleuven.be

[1]P. W. May, Philos. Trans. R. Soc. London A **358**, 473 (2000).

[2]T. Klein, P. Achatz, J. Kacmarcik, C. Marcenat, F. Gustafsson, J. Marcus, E. Bustarret, J. Pernot, F. Omnes, Bo E. Sernelius,

C. Persson, A. Ferreira da Silva, and C. Cytermann, Phys. Rev. B **75**, 165313 (2007).

[3]E. Bustarret, Phys. Status Solidi A **205**, 997 (2008).

[4]M. Stoneham, Nat. Mater. **3**, 3 (2004).

[5] Y. Takano, J. Phys. Condens. Matter **21**, 253201 (2009).

[6] E. A. Ekimov, V. A. Sidorov, E. D. Bauer, N. N. Mel'nik, N. J. Curro, J. D. Thompson, and S. M. Stishov, Nature **428**, 542 (2004).

[7] Y. Takano, M. Nagao, I. Sakaguchi, M. Tachiki, T. Hatano, K. Kobayashi, H. Umezawa, and H. Kawarada, Appl. Phys. Lett. **85**, 2851 (2004).

[8] M. Veres, S. Tóth, and M. Koós, Appl. Phys. Lett. **91**, 031913 (2007).

[9] D. M. Gruen, Annu. Rev. Mater. Sci. **29**, 211 (1999).

[10] S. Tomita, A. Burian, J. C. Dore, D. LeBolloch, M. Fujii, and S. Hayashi, Carbon **40**, 1469 (2002).

[11] O. A. Williams, M. Nesladek, M. Daenen, S. Michaelson, A. Hoffman, E. Osawa, K. Haenen, and R. B. Jackman, Diam. Relat. Mater. **17**, 1080 (2008).

[12] W. Gajewski, P. Achatz, O. A. Williams, K. Haenen, E. Bustarret, M. Stutzmann, and J. A. Garrido, Phys. Rev. B **79**, 045206 (2009).

[13] J. J. Mareš, P. Hubík, M. Nesládek, D. Kindl, and J. Krištofik, Diam. Relat. Mater. **15**, 1863 (2006).

[14] P. Achatz, W. Gajewski, E. Bustarret, C. Marcenat, R. Piquerel, C. Chapelier, T. Dubouchet, O. A. Williams, K. Haenen, J. A. Garrido, and M. Stutzmann, Phys. Rev. B **79**, 201203(R) (2009).

[15] J. J. Mareš, P. Hubík, J. Krištofik, and M. Nesládek, Phys. Status Solidi A **205**, 2163 (2008).

[16] B. L. Willems, G. Zhang, J. Vanacken, V. V. Moshchalkov, S. D. Janssens, O. A. Williams, K. Haenen, and P. Wagner, J. Appl. Phys. **106**, 033711 (2009).

[17] B. L. Willems, G. Zhang, J. Vanacken, V. V. Moshchalkov, I. Guillamon, H. Suderow, S. Vieira, S. D. Janssens, K. Haenen, and P. Wagner, Physica C **470**, 853 (2010).

[18] G. Zhang, J. Vanacken, J. Van de Vondel, W. Decelle, J. Fritzsche, V. V. Moshchalkov, B. L. Willems, S. D. Janssens, K. Haenen, and P. Wagner, J. Appl. Phys. **108**, 013904 (2010).

[19] B. L. Willems, G. Zhang, J. Vanacken, V. V. Moshchalkov, S. D. Janssens, K. Haenen, and P. Wagner, J. Phys. D: Appl. Phys. **43**, 374019 (2010).

[20] O. A. Williams, O. Douhéret, M. Daenen, K. Haenen, E. Ōsawa, and M. Takahashi, Chem. Phys. Lett. **445**, 255 (2007).

[21] S. D. Janssens, P. Pobedinskas, J. Vacík, V. Petráková, B. Ruttens, J. D'Haen, M. Nesládek, K. Haenen, and P. Wagner, New J. Phys. **13**, 083008 (2011).

[22] S. D. Janssens, P. Pobedinskas, V. Petráková, M. Nesládek, K. Haenen, and P. Wagner, MRS Proceedings 1282, mrsf10-1282-a15-04 doi:10.1557/opl.2011.454 (2011).

[23] P. W. May, M. N. R. Ashfold, and Y. A. Mankelevich, J. Appl. Phys. **101**, 053115 (2007).

[24] O. A. Williams and M. Nesládek, Phys. Status Solidi A **203**, 3375 (2006).

[25] B. L. Willems, V. H. Dao, J. Vanacken, L. F. Chibotaru, V. V. Moshchalkov, I. Guillamon, H. Suderow, S. Vieira, S. D. Janssens, O. A. Williams, K. Haenen, and P. Wagner, Phys. Rev. B **80**, 224518 (2009).

[26] B. L. Willems, Ph.D. thesis, ISBN 978-90-8649-236-7 (2009).

[27] F. Dahlem, P. Achatz, O. A. Williams, D. Araujo, E. Bustarret, and H. Courtois, Phys. Rev. B **82**, 033306 (2010).

[28] M. Saarela and F. V. Kusmartsev, in *Nanoscience and Engineering in Superconductivity*, edited by V. V. Moshchalkov, R. Wördenweber, and W. Lang, Springer Series in NanoScience and Technology (Springer-Verlag, Berlin Heidelberg, 2010), pp. 211–229, and references therein.

[29] B. Abeles, P. Sheng, M. D. Coutts, and Y. Arie, Adv. Phys. **24**, 407 (1975).

[30] B. Abeles, Phys. Rev. B **15**, 2828 (1977).

[31] Y. Shapira and G. Deutscher, Phys. Rev. B **27**, 4463 (1983).

[32] H. M. Jaeger, D. B. Haviland, B. G. Orr, and A. M. Goldman, Phys. Rev. B **40**, 182 (1989).

[33] R. W. Simon, B. J. Dalrymple, D. Van Vechten, W. W. Fuller, and S. A. Wolf, Phys. Rev. B **36**, 1962 (1987).

[34] N. F. Mott, J. Non-Cryst. Solids **1**, 1 (1968).

[35] C. Quitmann, D. Andrich, C. Jarchow, M. Fleuster, B. Beschoten, G. Güntherodt, V. V. Moshchalkov, G. Mante, and R. Manzke, Phys. Rev. B **46**, 11813 (1992).

[36] M. R. Graham, C. J. Adkins, H. Behar, and R. Rosenbaum, J. Phys. Condens. Matter **10**, 809 (1998).

[37] T. I. Baturina, A. Yu. Mironov, V. M. Vinokur, M. R. Baklanov, and C. Strunk, Phys. Rev. Lett. **99**, 257003 (2007).

[38] V. M. Vinokur, T. I. Baturina, M. V. Fistul, A. Yu. Mironov, M. R. Baklanov, and C. Strunk, Nature **452**, 613 (2008).

[39] M. V. Fistul, V. M. Vinokur, and T. I. Baturina, Phys. Rev. Lett. **100**, 086805 (2008).

[40] B. I. Shklovskii and A. L. Efros, in *Electronic Properties of Doped Semiconductors*, edited by M. Cardona, P. Fulde, and H. J. Queisser, Springer Series in Solid-State Sciences (Springer, Berlin, 1984), pp. 130–227, and references therein.

[41] D. Stauffer and A. Aharony, *Introduction to Percolation Theory*, (Taylor and Francis, London, 1992), pp. 89–95, and references therein.

[42] V. V. Moshchalkov and I. G. Muttik, Fiz. Tverd. Tela (Leningrad) **28**, 3750 (1986); Sov. Phys. Solid State **28**, 2114 (1986).

[43] V. V. Moshchalkov, *Advanced Solid State Physics*, lectures given at Katholieke Universiteit Leuven 2009 (unpublished), and references therein.

[44] A. F. Andreev, Sov. Phys. JETP **19**, 1228 (1964); **24**, 1019 (1967).

[45] Y. Aharonov and D. Bohm, Phys. Rev. **115**, 485 (1959).

[46] A. A. Bright, Phys. Rev. B **20**, 5142 (1979).

[47] B. L. Altshuler, D. Khmelnitzkii, A. I. Larkin, and P. A. Lee, Phys. Rev. B **22**, 5142 (1980).

[48] P. W. Anderson, Phys. Rev. **109**, 1492 (1958).

[49] Ad Lagendijk, B. van Tiggelen, and D. S. Wiersma, Phys. Today **62**, 24 (2009).

[50] D. Kalok, A. Bilušić, T. I. Baturina, V. M. Vinokur, and C. Strunk, [http://arxiv.org/abs/1004.5153] (2010).

[51] N. M. Chtchelkatchev, V. M. Vinokur, and T. I. Baturina, Phys. Rev. Lett. **103**, 247003 (2009).

[52] K. Fossheim and A. Sudbø, *Superconductivity: Physics and Applications* (John Wiley & Sons, Ltd., London, 2004), pp. 182–183.

[53] V. Buntar, M. Riccò, L. Cristofolini, H. W. Weber, and F. Bolzoni, Phys. Rev. B **52**, 4432 (1995).